Fuel Communications 12 (2022) 100074

Contents lists available at ScienceDirect

Fuel Communications

journal homepage: www.sciencedirect.com/journal/fuel-communications

Optical investigation and thermodynamic analysis of premixed ammonia dual-fuel combustion initiated by dodecane pilot fuel

Silas Wüthrich *, Patrick Cartier, Pascal Süess, Bruno Schneider, Peter Obrecht, Kai Herrmann

University of Applied Sciences and Arts Northwestern Switzerland (FHNW), Institute of Thermal and Fluid Engineering, Klosterzelgstrasse 2, CH-5210, Windisch, Switzerland

ARTICLE INFO

Keywords:
Ammonia
Experimental
Dual-fuel operation
Carbon free
Optical investigation
Retrofitting
Optical engine
Ignition delay

ABSTRACT

In view of reducing greenhouse gas emissions the transition from fossils fuels to sustainable energy carriers is a prerequisite to keep global warming within tolerable limits. Since IC engines will continue to play a role in global energy strategies during a transitional phase, especially for large engine applications difficult to electrify, the use of ammonia as substitute fuel may be an approach for decarbonization. However, its utilization needs research since ignition concepts and combustion properties still pose considerable challenges in view of reliable and efficient operation. A new "optical engine" test facility ("Flex-OeCoS") has been successfully adapted enabling dodecane pilot fuel ignited premixed ammonia dual-fuel combustion investigations. It features IC engine relevant operation conditions such as pressures, temperatures, and flow (turbulence) conditions as well as adjustable mixture charge composition and pilot fuel injection settings. In parallel, thermodynamic heat release analysis in terms of ignition and combustion characteristics was performed. Simultaneously applied high-speed Schlieren/OH* chemiluminescence measurements supported the examination of the combustion process. Initially premixed ammonia dual fuel combustion has been compared to a representative methane combustion process in terms of different gas properties (lower heating value, air-fuel ratio) which illustrates its lower reactivity affecting heat release and flame propagation. Moreover, ignition delay, combustion transition, and turbulent flame propagation as well as heat release characteristics have been investigated for premixed ammonia dual-fuel combustion within variation of air-fuel equivalence ratio, start of pilot fuel injection, and pressure/temperature operation conditions. The results illustrate strong dependency on air-fuel equivalence ratio (energy content) and temperature conditions in terms of ignition delay, dual-fuel combustion transition, and corresponding heat release. The optical investigations confirm the thermodynamic analysis and promote assessment of pilot fuel evaporation, ignition, combustion transition, and flame propagation. Conclusions give extended insight into the thermochemical processes of ammonia pilot fuel ignited dual-fuel combustion. The acquired data may also support further development of numerical CRFD methods.

Introduction

The Paris Agreement, a legally binding international treaty on climate change, aims at holding the increase in the global average temperature to well below 2 °C above pre-industrial levels and pursuing efforts to limit the temperature increase to 1.5 °C [1]. Consequently, the transition from fossil fuels to sustainable energy carriers is one of the necessities to keep global warming within tolerable limits. Reducing carbon intensity and total annual greenhouse gas emissions will be impossible without reverting to alternative fuels. Sustainable fuels can be generated either through synthesis based on renewable energy or from the processing of biological wastes and residues. The potential of biofuels is limited in terms of quantity, where synthetic fuels are associated with a price penalty depending on the refinement level.

Within global energy strategies IC engines will still play a role especially in terms of large engines for propulsion application or for

Abbreviations: aHRR, apparent heat release rate; aHR, apparent heat release; AFR, air-fuel ratio; s_{aFP}, Apparent flame propagation speed; CA, Crank angle; CFD, Computational fluid dynamics; CH_4, Methane; CI, Compression ignition; CR, Compression ratio; DI, Direct injection; DOI, duration of injection; DF, dual- fuel; GHG, greenhouse gas; IC, Internal combustion (engine); ID, Ignition Delay; IMO, International Maritime Organization; LBV, Laminar burning velocity; LHV, Lower heating value; LIV, Laser induced fluorescence; LPG, Liquefied petroleum gas; NH_3, Ammonia; RON, Research octane number; SOI, Start of injection; TDC, Top dead center.

* Corresponding author.
E-mail address: silas.wuethrich@fhnw.ch (S. Wüthrich).

https://doi.org/10.1016/j.jfueco.2022.100074
Received 25 February 2022; Received in revised form 13 June 2022; Accepted 1 July 2022
Available online 4 July 2022

decentralized power generation. As example, for future marine propulsion various technology pathways of IC engines and fuel systems have been investigated, where a substitution of fossil fuels with ammonia (or methanol) has been identified as an economically feasible route for decarbonization [2]. Current concepts of gas engines are seen as good basis for future solutions designed for operation on such alternative fuels, provided they are produced with electricity from renewable energy sources. Even though the ammonia fuel application is not new, the conversion of IC engines still providing comparable efficiency and guaranteeing reliable operation, poses certain challenges.

Ammonia, a colorless, poisonous gas, has been known to humanity since ancient times due to its pungent smell. But only with the advent of modern science in the 18th century it was firstly isolated as substance, soon after its molecular structure NH_3 was identified as well. With beginning of the use and production of synthetic fertilizers in the 19th century, interest in ammonia grew as possible source for nitrogen fixation. However, only after the invention of the Haber-Bosch process in the 1920s ammonia could be produced efficiently and in large quantities. By way of the Oswald process, invented some years before, ammonia could then be converted to nitric acid and used for the fertilizer production.

In 2020 about 175 million tons of ammonia have been produced as one of the most fabricated chemicals in the world [3]. Today, about 80% goes into fertilizer production, the rest is used as a base material for various industrial products and as a refrigerant. Almost all hydrogen used for ammonia production is coming from non-renewable sources (~70% from natural gas, ~20% from coal). However, by producing hydrogen with electrolysis, and by using newly developed ammonia synthesis processes, it is possible to produce "green" ammonia with efficiencies comparable or even better than the classical Haber-Bosch process [4,5].

Due to the scarcity of gasoline and diesel, ammonia was firstly used on a larger scale as a combustion engine fuel in the second world war [6]. Later in the 1960s, fear of possibly losing access to oil sources in times of crisis led to research activities on how gasoline and diesel fuels could be replaced. One of the promising candidates is ammonia, which was intensively researched in different IC engine types [7–10]. However, only in the last decades the need to become independent of carbon-based fuels led to renewed interest in ammonia, both as energy (hydrogen) carrier and as directly used fuel. As energy carrier ammonia has some striking advantages in comparison to hydrogen (which is the favored substitute for carbon-based fuels nowadays): Although the energy content by mass is far lower than for pure hydrogen, its heating content by volume is even higher than for liquid hydrogen (Table 1: LHV @ storage conditions). Heating content by volume is the challenging factor for vehicles, even ammonia needs about three times the volume of carbon-based fuels (identical efficiencies assumed) for the same range. However, hydrogen requires even more space – especially if the tank itself (for 70 MPa pressure, or −253 °C temperature) is calculated in. Further, a transport infrastructure for ammonia already exists, its handling is not much different than for LPG or propane. A disadvantage for applications requiring pure hydrogen is the fact that ammonia must be cracked beforehand which requires additional infrastructure [11,12]. Instead of extracting hydrogen before use, ammonia can be directly used as a fuel as well.

A comparison of ammonia with hydrogen and common carbon-based fuels is shown in Table 1. The low flame speed results in a slower combustion process in comparison to other fuels, which can reduce the combustion efficiency. The high auto-ignition temperature and enormous heat of vaporization makes liquid injection and diesel-like compression ignition combustion difficult. The high minimum ignition energy means that it is comparably more difficult to safely ignite an ammonia-air mixture. The high resistance to knocking (RON) allows to run ammonia fueled engines at higher compression ratios, which can be beneficial for efficiency. Although ammonia has a much lower energy content per mass than carbon-based standard fuels, its low stoichiometric air-fuel ratio *AFR* partly compensates this regarding the in-cylinder energy content.

Publications of research in the field of ammonia combustion in IC engines are far less numerous than for carbon-based fuels, an overview can be found in [4,13,18–20]. In the following only some important aspects regarding the work presented in this paper – pilot injection into a premixed ammonia-air charge – will be discussed.

In a *dual-fuel* combustion process a secondary more reactive fuel is injected separately into the engine cylinder to initiate ignition and promote combustion of the premixed charge. This combustion process is well established, especially for large engines running with natural gas. Both low-pressure port gas injection (in front of the intake valves) as well as high-pressure gas direct injection is applied. The latter, i.e. high pressure direct injection of both, (liquid) ammonia and pilot fuel, has so far been investigated in numerical studies only (except early experiments in 1966 [9]) to our knowledge [17,21]. The first method, where ammonia is mixed with air at low pressures before the intake valves, has been investigated more often. Already in 1967 it was seen that this mode of operation works well and can result in even higher power output and efficiency compared to pure diesel operation due to the high necessary air excess for diesel [10]. Since then, IC engine technology has developed significantly, offering new ways on how to control respectively influence the combustion process, as for example the common rail injection technique which provides full freedom regarding injection pressure, quantity, and timing.

In [22] a 4.5-liter four-cylinder turbocharged DI diesel engine (CR 17) with a common rail fuel injection system was converted for ammonia admission in the intake manifold. The engine operated successfully with up to 95% of the fuel energy provided by ammonia. Best

Table 1
Properties of ammonia and other fuels suitable for IC engines. Data collected for comparison only from [13–18].

Fuel	Ammonia (Liquid) NH_3	Hydrogen (Liquid)	Hydrogen (Compressed) H_2	Methane (acCompressed) CH_4	IsoOctane (Gasoline) C_8H_{18}	n-Dodecane (Diesel) $C_{12}H_{26}$
Storage conditions	1.1 MPa/300 K	0.1 MPa/20 K	70 MPa/300 K	25 MPa/300 K	0.1 MPa/300 K	0.1 MPa/300 K
Density @ storage conditions	600 kg/m^3	71 kg/m^3	39 kg/m^3	187 kg/m^3	700 kg/m^3	750 kg/m3
LHV @ storage conditions	18.8 MJ/kg 11.3 GJ/m^3	120 MJ/kg 8.5 GJ/m^3	120 MJ/kg 4.7 GJ/m^3	50 MJ/kg 9.4 GJ/m^3	44 MJ/kg 31 GJ/m^3	45 MJ/kg 33 GJ/m^3
Flammability limits in air	15 – 28 Vol-%	4.7 – 75 Vol-%		5 – 15 Vol-%	0.9 – 6 Vol-%	0.6 – 7.5 Vol-%
Stoichiometric AFR (mass)	6.1 : 1	34.3 : 1		17.3 : 1	~ 15 : 1	~ 15 : 1
LHV per Volume @ stoichiometry (0.1 MPa, 373 K)	~ 2.23 MJ/m^3	~ 2.30 MJ/m^3		~ 2.45 MJ/m^3	~ 2.71 MJ/m^3	–
Auto-ignition temperature	930 K	773 – 850 K		860 K	670 K	480 K
Minimum ignition energy	8 mJ	~ 0.016 mJ		~ 0.21 mJ	1.35 mJ (Gasol. ~0.14 mJ)	(Diesel ~0.23 mJ)
Heat of vaporization	1370 kJ/kg					256 kJ/kg
LBV @ stoichiometry (0.1 MPa, 300 K)	0.07 m/s	3.5 m/s		0.38 m/s	0.4 m/s (Gasol. ~0.6 m/s)	~ 0.8 m/s
RON	> 130	> 100		120	100	–

overall fuel efficiency (38.5%) was achieved with a content of 60% ammonia. Both normal diesel and biodiesel have been tested as pilot fuel, no difference could be observed. The study presented in [23] used the same engine but equipped with a standard fuel injection system. The best overall fuel efficiency resulted from an ammonia energy content of 40% to 60%. High ammonia content results in longer ignition delays, lower peak pressures, and combustion durations. Very low ammonia energy contents resulted in too lean mixtures that would not burn. The publications [24,25] confirmed the findings – higher amounts of ammonia increase ignition delay and reduce peak cylinder pressure. In addition, different pilot injection strategies to reduce emissions were investigated. In [26] timing of the diesel pilot injection was examined in a 2.44-liter single cylinder engine with variable ammonia content. High amounts of ammonia (up to 40% of the total energy) with optimized diesel injection timing reduced total greenhouse gas emissions by 12%. A follow-up study [27] used split diesel injections for further optimizations. This improved the reduction of the total greenhouse gas emissions to 30% compared to pure diesel operation. Further, it also reduced ammonia exhaust emissions by more than 80% compared to the single injection strategy.

Emissions are not measured in the present work, but general trends can be observed from literature. *Ammonia*: Due to crevice volumes in the engine and long quenching distance some of ammonia contained in the in-cylinder mixture is inevitably emitted into the exhaust. In general, higher ammonia content (i.e. richer mixtures) results in higher emissions, but a "hotter" faster combustion – also achievable by mixing with a more reactive fuel like hydrogen – lowers those emissions. *Nitric oxides, dioxides*: As in all IC engines, thermal NO_X is produced in hot combustion zones. For ammonia however, the bound nitrogen atom in the fuel also leads to NO_X production from combustion itself, so engines can emit high NO_X levels even if combustion zones have comparably low temperatures. *Nitrous oxide*: Ammonia fueled IC engines can emit N_2O, especially if combustion temperatures are low [28]. However, N_2O emissions should be avoided because it is a long-lived greenhouse gas with a global warming potential about 265 times higher than CO_2. *Unburned hydrocarbons, carbon monoxide, carbon dioxide*: In dual-fuel IC engines the pilot fuel usually contains carbon, therefore engine emissions will include HC, CO, CO_2, and possibly soot. Reduced combustion temperatures with ammonia can lead to even higher HC and CO emissions in comparison to pure diesel operation. However, if the liquid fuel injection is only used to ignite the premixed charge, then the very small amounts of pilot fuel are expected to lower the emission levels in comparison to pure diesel operation. *Hydrogen*: H_2 is not a pollutant, but also emitted even if the engines operate with pure ammonia. Most likely it is produced from ammonia dissociation during compression which is then trapped in crevices.

The usage of ammonia as fuel in IC engine application needs further investigation since ignition concepts and combustion properties still pose considerable challenges in view of reliable operation. A range of involved complex processes such as flow field conditions, evaporation and mixing properties, ignition, combustion onset, and flame propagation need to be considered. In addition, ammonia slip and GHG emission in the exhaust gas must be avoided.

In combustion research investigation by means of optical diagnostics is an important tool for essential insight. In this work, an optically accessible experimental test facility providing engine relevant operation conditions was used to fundamentally examine premixed pilot fuel ignited ammonia dual-fuel combustion. The investigations include levels of typical operating conditions for marine dual-fuel engines with compression temperatures around 800 K and peak pressures up to 180 bar and beyond. The influence of different operation parameters, such as mixture charge composition or process temperatures and pressures has been investigated in initial measurement campaigns. A first aim is to demonstrate the applicability of the test rig as well as of the optical diagnostics regarding basic investigations of ammonia combustion. Moreover, first insight into the thermo-chemical processes of ammonia combustion in terms of ignition delay, combustion onset, dual-fuel combustion transition, turbulent flame propagation, and heat release shall be provided.

Experimental setup

Experimental test facility "Flex OeCoS"

The optically accessible test facility "Flex-OeCoS" enables examination of premixed pilot fuel ignited dual-fuel combustion processes in a range of IC engine relevant operational parameters [29]. Its working principle is illustrated in Fig. 1: One cylinder of a motor driven engine block feeds a mixture charge into an optical combustion chamber.

The distinctive cylinder head, shown in Fig. 2 is equipped with rectangular and round sapphire windows at each side providing full optical access (covering the chamber walls) of the Ø60 mm × 20 mm combustion chamber. Two intake valves (Ø16 mm, one of those recognizable in Fig. 2 right) are located on the working cylinder, which is equipped with a flat-top piston. Two exhaust valves (Ø16 mm) are positioned on top of the combustion chamber, where a central bore at the top allows mounting of a pilot fuel injector, spark plug or prechamber. Various pressure sensors are implemented at different locations, and the entire head is thermally conditioned to achieve stable conditions during the aperiodic operation.

Initially, precise acquisition of crank-angle resolved operating condition has been investigated. Finally, the turbulent flow field by means of high-speed PIV was determined [29] as well as the pressure measurement procedure (i.e. sensor thermal conditioning) could be established, and the working gas temperature by pure air compression has been acquired by means of fine-wire thermocouples at different locations [29,30].

The Flex-OeCoS test facility features adaptable operation at IC engine relevant conditions: peak pressures of up to 240 bar (from boost-adjustable compression pressure p_c up to 130 bar), mixture charge temperatures T between 700–1000 K by inlet conditioning, and tunable flow (turbulence grades) depending on motor speed n of typically 300–1000 rpm. An overview of relevant test facility specifications is given in Table 2.

Independent pneumatic intake and exhaust valve drives ensures high variability. Moreover, pilot fuel injection settings (pressure, start, and duration) as well as mixture charge composition, by gas introduction in the air inlet pipe close to the intake valve, can be freely set by external supply units. The adaptable setup with flexible operation modes has already been used for different dual-fuel combustion process investigations [31,32].

Optical setup, methodology, and post-processing

As illustrated in Fig. 3, simultaneous high-speed Schlieren/OH*

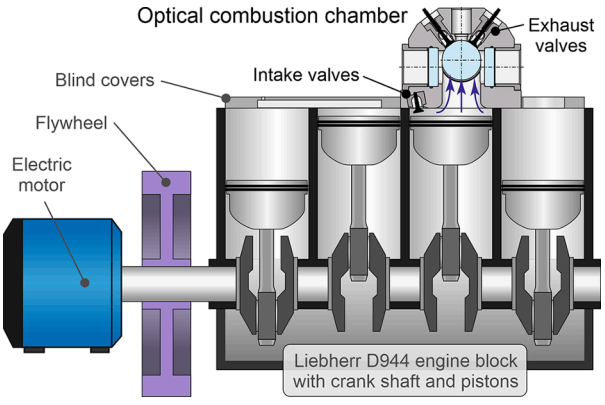

Fig. 1. Concept of the "Flex-OeCoS" test facility.

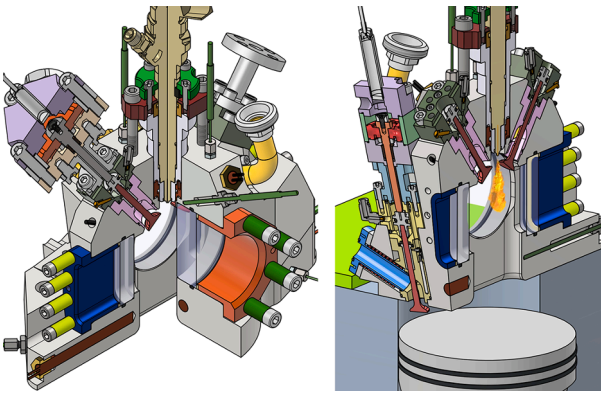

Fig. 2. Cylinder head on the working cylinder with optical combustion chamber, intake/exhaust valves, and centered pilot fuel injector.

Table 2
Test facility specifications.

Dimensions, Operating Parameter		
Working cylinder bore	Ø 130	[mm]
Stroke length	150	[mm]
Connecting rod length	237.1	[mm]
Displacement (working cylinder)	1990	[cm^3]
Compression ratio	13.8	[-]
Combustion chamber diameter/height	60/20	[mm]
Max. cylinder pressure	240	[bar]
Motor speed range	300 - 1000	[rpm]

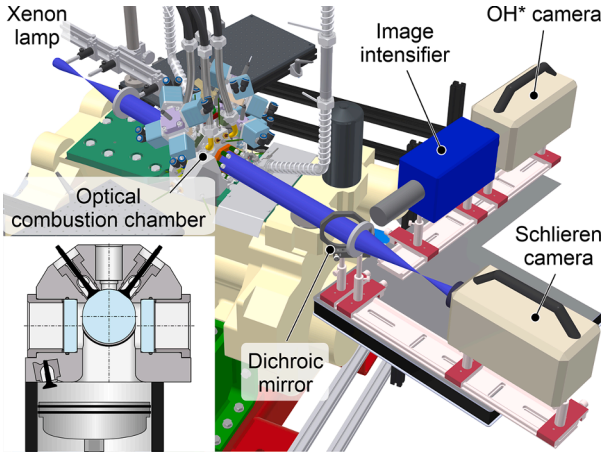

Fig. 3. Optical setup of simultaneously applied Schlieren and OH* chemiluminescence measurement techniques.

chemiluminescence was applied to investigate pilot fuel injection and evaporation, dual-fuel ignition processes, turbulent flame front propagation, and combustion characteristics.

In the Schlieren setup, light from a xenon lamp is guided to an aperture acting as point light source. The achromatic lens ($f = 200$ mm) afterwards generates a collimated light beam passing through the combustion chamber. A pinhole aperture enables the Schlieren sensitivity adjustment. Image acquisition was performed by means of a high-speed camera (Nova S12, Nikkor 35 mm $f^{\#}$ 2). A dichroic mirror mounted under 45° in the optical main axis is reflecting the UV part (around 308 nm). Thus, the chemiluminescence of the OH* radical as indicator of inflammation was acquired simultaneously with a second high-speed camera (Nova S12) coupled to a high-speed image intensifier (IRO X, Sodern Cerco 45 mm $f^{\#}$ 1.4) and a 308 nm narrowband filter to pass only the radiation corresponding to the OH* radical, respectively. Image acquisition is synchronized to the crank shaft angle encoder. Spatial resolution of the high-speed cameras has been set to 60 × 60 mm (covering the entire combustion chamber) to achieve a temporal resolution of 0.1 °CA, for the typical motor speed of $n = 600$ rpm, resulting in a frame rate of 36 kHz.

Fig. 4 exemplarily shows a pilot fuel ignited lean-premixed methane/air charge measurement [31]. The resulting images (overlay of both specific recordings) illustrates the evaporating spray (Schlieren) simultaneously with starting "chemical reaction" (OH* signal colorized magenta), and recognizable flame propagation. To evaluate ignition delay *ID* optically, start of injection *SOI* and combustion onset must be quantitatively analyzed in a post-processing procedure.

The determination of *SOI* is based on the Schlieren spray contour. Due to high turbulence levels, a detection of the spray/flame with a threshold value often leads to errors. Thus, detection is based on a predefined probability density function dependent on the image zone (background, dense core, flame) to assign pixel values to a specific location. However, even highest camera frame rates never facilitate a systematic capture of every actual injection begin, since it cannot be accurately timed due to the inherent slightly deviating hydraulic delay of the injector. According to the realistic assumption that the spray area increases linearly at first, the effective start of injection was extrapolated from evaluated spray area values.

The OH* chemiluminescence corresponds to ignition and represents an integrated line-of-sight signal along the entire measurement volume. Even though other species (e.g. CO_2*), particularly under lean conditions at high pressures, may contribute considerably to the overall OH* signal at progressing combustion [33,34], the first OH* chemiluminescence emission appears at least simultaneously at ignition [35]. Moreover, also the interference of soot incandescence does not (yet) affect the ignition detection [36]. The start of (high temperature) combustion can be defined as the first OH* appearance, respectively the first image containing a "brighter spot" – as previous studies have shown that OH* is a suitable tracer for determination of ignition onset [37,38]. Different approaches were implemented in the image post-processing procedure: First, ignition has been identified if an area >15 pixel has a higher gray level value than a certain threshold value. The latter is calculated out of the maximum and the standard deviation value of the first couple of images and a user-defined factor. This approach works properly if the flame size increases fast enough after ignition. Though, if the core of OH* intensity increases slowly, a second approach was implemented, dividing the image into smaller sub images, and analyzing the noise distribution. More precisely, it counts the values that differ from the median by a certain amount. In a next step, the range of this value between all the sub images is calculated. The ignition has started, if this range is higher than a threshold, which is determined out of the median range of the first couple of images and a user-defined factor. If both approaches deliver plausible solutions, the smaller analyzed ignition delay value is used for further processing. At last, the automated ignition delay detection by means of these simultaneously applied approaches was reliable, also compared to the corresponding heat release analysis.

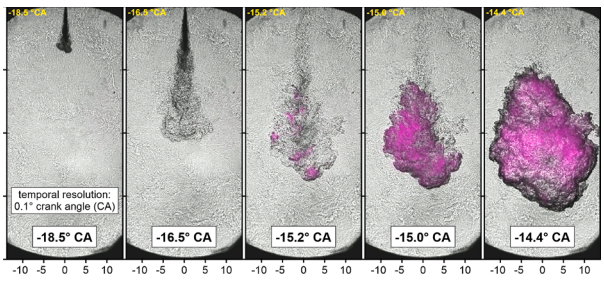

Fig. 4. Exemplary sequence of OH*/Schlieren recordings overlayed to examine spray evaporation, ignition, and flame propagation.

Operation conditions, measurement process, and analysis procedures

In a standardized preparation procedure, one hundred motored compression/expansion cycles (720 °CA as a 4-stroke engine) are required – where 0 °CA corresponds to firing top dead center (*TDC*) and 360 °CA to gas exchange *TDC* – to achieve steady operation conditions prior to experimental cycles. The latter consist of one combustion cycle followed by five scavenging cycles, which are necessary to achieve complete flushing of the combustion chamber because of the relatively small intake valves due to optimization in terms of optical accessibility. During the measuring process a series of experimental cycles are performed where typically the last twenty-five combustion cycles (after achieving close to steady conditions) will be analyzed. Cycle-resolved operating process data, test facility boundary conditions, and associated high-speed camera recordings are handled by an automated processing tool. Moreover, it yields an initial on-site analysis of pressure, temperature, and mass flow peak/mean values as well as cycle-to-cycle variation, ignition delay, heat release, and other metrics to assess the integrity of the experiment.

Ammonia has been supplied from a 10-liter pressure bottle (covered by 50 °C heating jacket) through a pressure reduction valve via heated separate supply line (still at 50 °C) at about 9 bar to avoid condensation based on the vapor pressure characteristics. The feed into the inlet pipes in front of the two intake valves was realized by a specially designed intermediate piece containing four commercial (automotive) natural gas injectors per air feed line. Since those originally are not made for ammonia use, they needed to be exchanged after a certain operation duration due to sealing issues – a proper ammonia gas injector for upcoming investigations is in evaluation. The air-fuel equivalence ratio is determined using specifically calibrated Coriolis flowmeter instruments, which separately acquire mass flow of ammonia and air, respectively. To ensure the insertion of sufficient mass in short time and to optimize mixing behavior ammonia was already admitted into the inlet pipe in front of still closed intake valves at 160 °CA before gas exchange *TDC* (correspondingly −520 °CA before firing *TDC*) during the gas exchange preparation cycles. Pressure level of ammonia supply around 9 bar is in any case higher than intake boost pressure p_b.

Table 3 shows the test facility parameter settings based on pure air compression, such as intake temperature T_{in}, intake boost pressure p_b with subsequent compression pressure p_c, and flow field (turbulence intensity u') conditions established by the motor speed n. These settings are denoted as reference values for any gas/air pilot fuel ignited dual-fuel investigations, where certain parameters (e.g. effective compression pressure/temperature) are dependent on the specific gas respectively mixture charge properties.

The stated turbulence intensity u' is a characteristic value on comprehensive flow field investigations in the combustion chamber by means of high-speed PIV [29]. The measurement data was exploited to ensemble-averaged velocity fields as well as to achieve information on large-scale fluctuations and cycle-to-cycle variation. The associated turbulent kinetic energy of this differentiated flow fields was analyzed. At last, operating point associated characteristic values (ensemble averaged mean velocity, area averaged turbulence intensity) as indicator of the flow/turbulence conditions were determined.

Since the turbulent flow field also leads to non-uniform temperature distribution another characteristic value for a temperature designation needs to be defined. Process gas temperature by pure air compression temperature has been evaluated by means of fast fine-wire thermocouple measurements with different diameters which allows a determination of the response time [29,30]. In total, twenty-one measurement locations – at seven positions distributed in the circular combustion chamber area within the center plane and in planes shifted ±5 mm in depth – were examined. The interpolation of values between top and center position, in the region where the pilot fuel ignites, has been assigned as the compression temperature. The results of pure air compression based on the measurements show an excellent agreement to a thermodynamic analysis (see Fig. 5 below). Thus, methane and ammonia mixture compression temperatures have been determined correspondingly taking gas respectively mixture properties (e.g. heat capacity coefficients) into account. Of course, the designated values at start of injection must be interpreted somewhat with caution. Nevertheless, a best possible definition is given, and relative temperature differences can be considered as accurate.

Table 4 gives an overview of operation settings of the performed measurements in terms of ammonia/air mixture charge conditions such as air-fuel equivalence ratio λ, start of pilot fuel injection *SOI*, and noting that the subsequent compression pressure p_{c_NH3} and temperature T_{c_NH3} is depending on parameter settings.

Table 5 shows the variation of settings for the dodecane pilot fuel injection (Bosch CRI-2 solenoid injector) through a ∅90 µm single-hole nozzle. Injection pressure, start and duration (based on initially determined injection rate characteristics according to energizing time) can be set independently by a separate fuel supply unit. However, the results presented here refer to a constant injection duration *DOI* only to allow an evaluation of other operating parameters unaffected by this.

Start of injection, ignition delay (location), combustion onset, and flame propagation has been evaluated by post-processing procedures of the simultaneously applied Schlieren and OH* chemiluminescence measurements described above. In addition, a comprehensive analysis of the combustion process measurements has been performed to determine heat release rate as well as to assess ignition and combustion characteristics compared to optical diagnostics correspondingly.

The combustion heat release rate has been analyzed based on the pressure measurements applying an in-house thermodynamic 2-zone model considering dissociation in the burnt gas zone, and accounting for losses by wall heat transfer, piston ring blow-by, and crevice volumes [39]. Due to the unique test facility layout (with an optical combustion chamber connected to a working cylinder), significant efforts were made in terms of high precision pressure acquisition: proper sensor selection,

Table 3
Test facility parameter settings.

Reference values (air charge)		
Intake boost pressure p_b	2.65/4.4/5.8	[bar]
Compression pressure p_c	70/100/130	[bar]
Intake temperature T_{in}	50/100	[°C]
Motor speed n	600	[rpm]
Turbulence intensity u' [29]	3.6	[m/s]

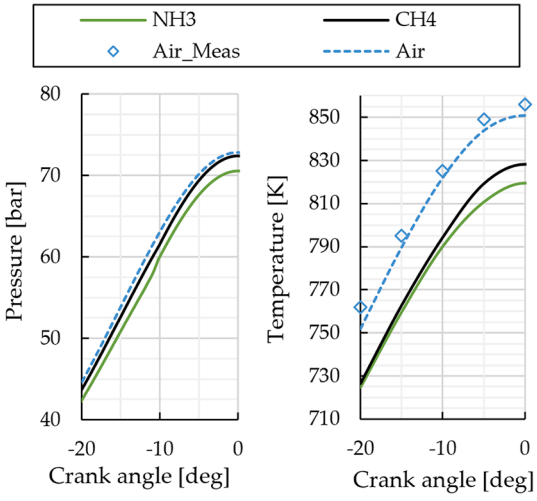

Fig. 5. Compression pressures (measured) and temperatures (calculated) of air (incl. measurement) vs. methane respectively ammonia mixture charges with λ = 1.5 at operating parameters p_c = 70 bar, T_{in} = 50 °C.

Table 4
Measurement operation parameter settings.

NH_3/air mixture charge		
Air-fuel equivalence ratio actλ	2.0/1.75/1.5/1.25/1.0	
Start of injection (*SOI*)	−20/−15/−10/−5/0	[°CA]
Compression pressure p_{c_NH3}	*setting dependent* → see results	[bar]
Compression temperature T_{c_NH3}	*setting dependent* → see results	[K]

Table 5
Pilot fuel injection parameters settings.

Pilot fuel injection parameters		
Pilot fuel	Dodecane	
Nozzle diameter d_{nozzle}	Ø 90	[µm]
Injection pressure p_{inj}	1000	[bar]
Start of injection *SOI*	−20/−15/−10/−5/0	[°CA]
Energizing time *ET*	500	[µs]
Duration of injection *DOI*	523	[µs]
DOI based on ET according to experimental injection rate analysis		

positioning, and thermal conditioning as well as piezo-electric sensor (relative) pressure "pegging" calibration procedure using piezo-resistive sensor (absolute) pressure measurements [30]. Piston-ring blow-by was measured (verifying typical values of 1–2% of mass flow) and the volume of crevices were determined by design drawings and tolerances. The wall heat losses were estimated using an adapted *Woschni* approach. An extended heat transfer coefficient α_W was developed taking flow measurements (turbulence analysis) inside of the combustion chamber into account [30]. However, since the wall-heat loss model had to be tuned by distinctive constants the results are denoted as apparent heat release rate *aHRR*. This estimated heat release of pilot fuel ignited lean-premixed methane dual-fuel investigations is in good agreement with corresponding CFD [40].

Ignition delay can be deduced from both optical data (OH* chemiluminescence) and from the calculated heat release rates (the effective start of injection SOI has been determined from optical data). The total energy available for combustion is the sum of the energy content in the injected pilot fuel and the energy contained in the premixed cylinder charge. By assuming that the pilot spray energy content has been unleashed completely before the main charge starts to burn it is possible to define a threshold level of the heat release that marks the onset of the premixed mixture combustion. This delay between ignition and the moment when the heat release is exceeding the energy content of the injected pilot fuel is denoted as transition time. The energy from the premixed charge entrained in the evaporating fuel spray and combusting together with it is not considered in this definition. Therefore, the longer the ignition delay, the larger the amount of premixed charge combusting together with the pilot fuel, and the more the transition time underestimates the time required to burn the complete evaporated fuel spray volume. Nonetheless this time is an important value to characterize dual fuel combustion and reflects the reactivity at the temperature/pressure conditions during inflammation.

An apparent flame propagation speed s_{aFP} can be evaluated out of the optical Schlieren measurements with different approaches. In any case, the Schlieren contour displacement representing the flame surface must be determined by geometrical or fractal analysis, still containing certain uncertainty in differentiation of refractive index variation based on reactive zone or local transport phenomena (flow/turbulence, diffusion) effects. The method applied consists of a two-dimensional spatially averaged evaluation of reaction zone expansion based on the optical measurements. It resolves local behavior very well (i.e. large propagation speeds) but is also more prone to misidentification of burned zones. However, the chosen approach in the context of these evaluations can make a precise statement when it comes to the start of combustion. The designation "apparent" shall point out that the analyzed flame propagation speed must be interpreted as a qualitative value nevertheless enabling a comparison within operation parameter variation.

Results

The dual-fuel combustion principle is a complex process. Starting with a mixture charge admission followed by typically liquid pilot fuel injection with subsequent evaporation and mixing, a two-stage ignition process is initiated: first auto-ignition based on pilot fuel properties and operation conditions, followed by a combustion transition in terms of an inflammation of the premixed gas/air charge, finally leading to a propagating turbulent premixed flame.

In view of ignition behavior of dual-fuel combustion processes, a distinction must be made between the so-called low-temperature reactivity and the high-temperature ignition – the latter investigated here by means of OH* chemiluminescence. An excellent overview of fundamental processes going on – though for low pressures and quiescent flow conditions – is given in [35]. In an own study it was possible to detect low-temperature ignition with formaldehyde as tracer to examine low-T reactivity by means of CH_2O-LIF in the Flex-OeCoS [31]. But for thermo-physical properties closer to IC engine relevant conditions, its occurrence as short-lived chemical intermediate species decreases due to higher pressures and especially the presence of turbulent flow affecting the mixing process. Thus, the ignition delays here at IC engine relevant elevated pressures refer to the high temperature ignition examined by means of OH* chemiluminescence. On the other hand, the characteristic disappearance of the Schlieren signal – attributed to heat release of first stage ignition compensating the refractive index change due to fuel evaporative cooling – could also be used as a proxy indicator for low-T reactivity/ignition before high-temperature ignition takes place [41]. Thus, the Schlieren contrast diminishment in the presented results qualitatively also marks the low-temperature ignition stage.

A first insight into the thermo-chemical processes of ammonia combustion in terms of ignition delay, combustion onset, dual-fuel combustion transition, turbulent flame propagation, and heat release is presented in the following sections.

Comparison of methane vs. ammonia dual-fuel combustion

In view of experiences gained in former premixed, pilot fuel ignited methane dual-fuel investigations [31,40] it is of interest to compare those measurements with the new ones using ammonia instead of methane as main fuel. The measurement conditions for the comparison correspond to the reference test facility parameters shown in Table 3 (compression pressure $p_c = 70$ bar, intake temperature $T_{in} = 50$ °C). Fig. 5 shows measured compression pressures (left) and estimated compression temperatures (right) for an air-fuel equivalence ratio of $\lambda = 1.5$. The fine-wire thermocouple measurements (as explained before) for pure air compression are shown as well, they correspond well to the thermodynamic calculation of the compression temperature. Similarly appropriate temperature/pressure/gas mixture dependent thermal gas properties respectively specific heats were used to calculate the estimated methane respectively ammonia charge mixture temperature. Whereas the pressures do not deviate much from the pure air case, the temperature at the start of the pilot injection ($SOI = -15$ °CA) is about 30 °C lower for both the methane and the ammonia case.

Fig. 6 shows a comparison of the pressure development for a methane vs. an ammonia charge mixture in the optical combustion chamber. The dodecane pilot fuel injection with an energizing time of $ET = 500$ µs, was initiated at $SOI = -15$ °CA, corresponding to a compression temperature of about 760 K for both methane and ammonia. The pressure trace represents the averaged value of twenty-five subsequent cycles superimposed by the standard deviation (*STD*), which reveals slightly higher cycle-to-cycle variation in the ammonia combustion case.

In terms of energy respectively heat release, two aspects must be considered. On the one hand, the specific heating value of ammonia is

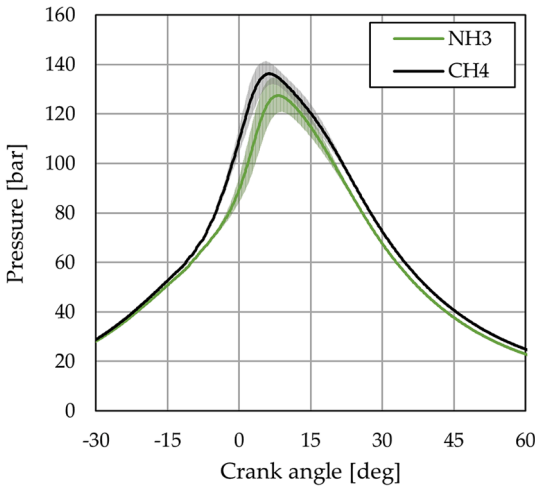

Fig. 6. Pressure traces of pilot fuel ignited ammonia vs. methane DF combustion (incl. *STD* of 25 cycles) at operation parameters $p_c = 70$ bar, $T_{in} = 50$ °C, $\lambda = 1.5$, $SOI = -15$ °CA, $ET = 500$ µs.

less than half compared to methane (Table 1, *LHV*: 18.8 MJ/kg vs. 50 MJ/kg). On the other hand, for stoichiometric combustion ammonia needs less air (Table 1, *AFR*: 6.1 vs. 17.3) than methane. Ultimately, the (constant) mixture charge volume in the Flex-OeCoS test facility during an experimental cycle leads to slightly less energy content of ammonia vs. methane combustion. Thus, for an air-fuel equivalence ratio of $\lambda = 1.5$, the energy content of the ammonia/air mixture is 4.6% lower than the one for the methane case. Fig. 6 shows measured pressures of the comparison case.

Assuming identical combustion conversion rates, peak pressures only depend on energy amount and position of the center of combustion. Regarding the above statements in terms of LHV respectively AFR, peak pressure of ammonia is slightly lower than for methane as expected. The lower pressure rise rate of ammonia, due to lower reactivity, shifts the center of combustion to a later position.

In Fig. 7 the apparent heat release rates for the two cases are shown. The *aHRR* for methane rises much earlier and faster than for ammonia as indicated by the corresponding pressure traces in Fig. 6. However, both peak heat release rates and its maximum gradients are not much different for the two cases. For methane, a distinct two-phase heat release can be observed, which is also present but far less obvious for ammonia. This two-phase heat release is due to the special design of the test facility (as shown in Fig. 2.): The tilted optically combustion chamber is fed by the working cylinder underneath, those two connected volumes cause a "staged" combustion process. In the beginning, the flame can expand freely in the optically accessible combustion chamber. Subsequently, when it reaches the bottom of the chamber, it propagates down through the narrow connection to the engine cylinder to combust the charge there.

The separate combustion process in the optical chamber and in the working cylinder underneath causes the two-phase heat release. This effect is more pronounced for fast *aHHR*, because for slower combustion processes, the combustion in the optical chamber and in the working cylinder overlap, which renders the staged combustion process much less obvious.

Due to this "staged combustion" in the Flex-OeCoS, IC engine typical values which describe the burning behavior in later combustion phases, such as burned mass fraction at 50/90% (MBF50/MBF90), cannot be compared to measurements in this test facility, which was optimized for optical investigation of ignition, combustion onset, and the early flame propagation process.

The ignition and early combustion process is shown in detail in the apparent heat release rates in Fig. 8. The ignition delay of the injected dodecane ($SOI = -15$ °CA) is quite similar for both cases. The initial *aHRR* for the methane case rises faster than for ammonia, which points to a higher reactivity of the air/methane/dodecane mixture. After the initial rise both cases reach a pedestal of an approximately constant heat release rate around $SOI = -10$ °CA. For methane, the delay until the *aHRR* rises again (due to the inflammation of the premixed charge) is much shorter than for ammonia, which again reflects the higher reactivity of the methane/air mixture.

The simultaneously performed Schlieren/ OH* chemiluminescence measurements as exemplarily shown in Fig. 9 complement the assessment of the dual-fuel ignition and combustion process by pressure and heat release analysis. The resulting images are overlays of the two simultaneously acquired recordings, one illustrating the liquid spray penetration and its evaporation from the Schlieren measurement, the other showing the starting "chemical reactivity" from the OH* chemiluminescence acquisition – colorized magenta for methane, green for ammonia. Note that not the entire sequence with a temporal resolution of 0.1 °CA is displayed but just representative timings.

The subsequent processes of pilot fuel injection (from the top) at −14.7 °CA ($SOI = -15$ °CA), pilot spray evaporation and ignition (approximately at −12.7 °CA for methane or between −11.7 and −10.7

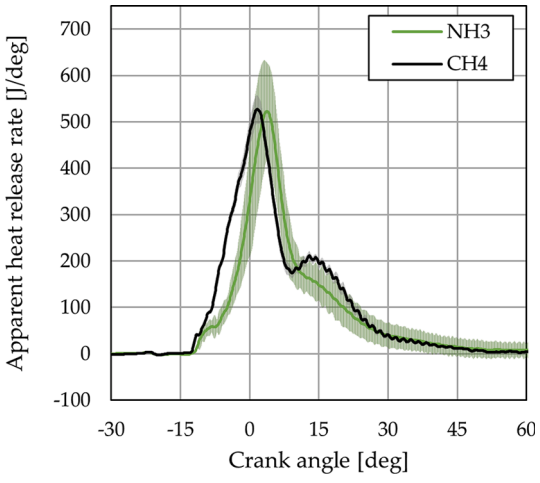

Fig. 7. Apparent heat release rate *aHRR* of pilot fuel ignited ammonia vs. methane DF combustion at operation parameters $p_c = 70$ bar, $T_{in} = 50$ °C, $\lambda = 1.5$, $SOI = -15$ °CA, $ET = 500/600$ µs (NH_3/CH_4).

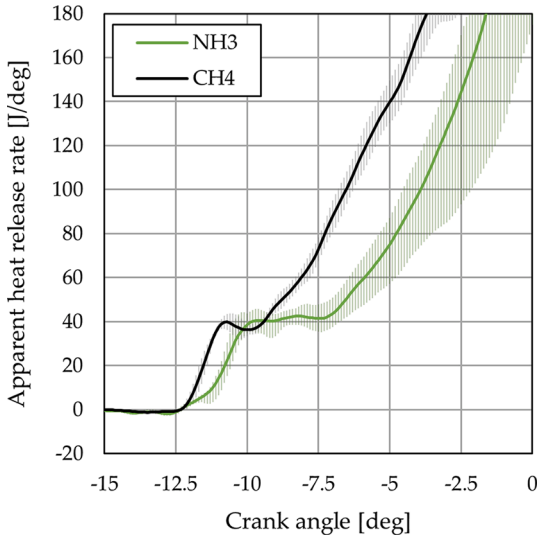

Fig. 8. Apparent heat release rate *aHRR* of pilot fuel ignited ammonia vs. methane DF combustion at operation parameters $p_c = 70$ bar, $T_{in} = 50$ °C, $\lambda = 1.5$, $SOI = -15$ °CA, $ET = 500/600$ µs (NH_3/CH_4).

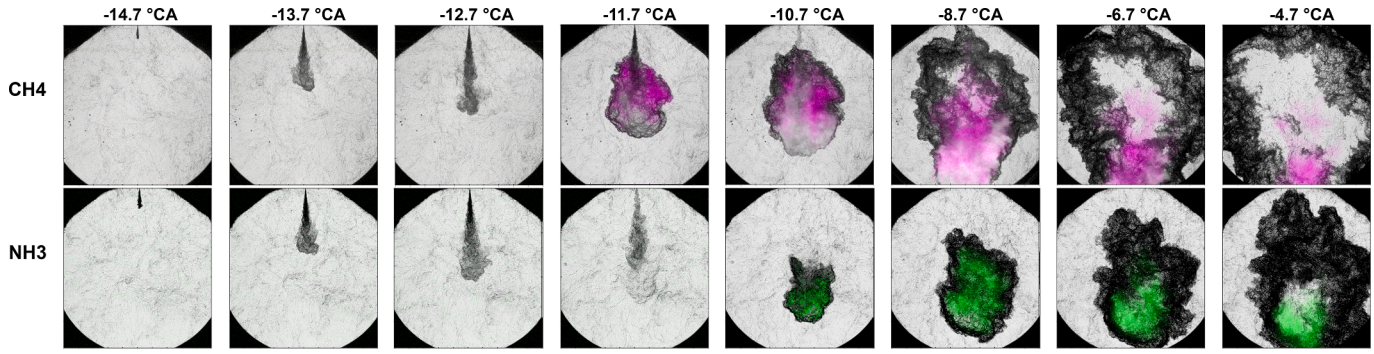

Fig. 9. Image sequence of overlayed simultaneously acquired high-speed Schlieren/OH*chemiluminscence (CH_4 magenta; NH_3 green) recordings of pilot fuel ignited ammonia vs. methane DF combustion at operation parameters p_c = 70 bar, T_{in} = 50 °C, λ = 1.5, *SOI* = −15 °CA, *ET* = 500/600 µs (NH_3/CH_4).

°CA for ammonia), the combustion transition into the premixed mixture charge (starting around −10.7 °CA for methane, respectively −8.7 °CA for ammonia), and the following flame propagation through the combustion chamber are well recognizable. Further, the "white" areas in the methane image sequence (between −10.7 °CA to −8.7 °CA) are an indication of soot formation in the pilot fuel spray tip (due to interference of soot incandescence with the OH* chemiluminescence signal [31]) during the combustion transition process where fuel rich zones favor soot production. Since ammonia does not contain any intermolecular carbon, and the evaporated pilot fuel spray does not form fuel rich zones, soot production cannot be observed in the ammonia case. The combustion transition time of about 2 °CA for ammonia, as seen in the *aHRR* analysis (Fig. 8), is confirmed by the optical measurements. The faster flame evolution in the methane case (−10.7 to −4.7 °CA) is in correspondence with the faster rise of the *aHRR* shown in Fig. 7.

Pilot fuel spray evolution (penetration, angle) and spray morphology (liquid core, evaporated zones) have been analyzed for the methane case [42]. In addition, the well observable growth of the reactive zone in the images can be used to determine an apparent flame propagation speed (see section 2.3). For the ammonia case, results of this analysis in terms of variation of the air-fuel equivalence ratio (Fig. 13) respectively temperature at *SOI* (Fig. 21) are presented in the following sections 3.2 and 3.3. A comprehensive comparison of pilot fuel ignited methane vs. ammonia dual-fuel combustion in view of a publication is in consideration.

Variation of air-fuel equivalence ratio

In IC engines, the air-fuel equivalence ratio can be adjusted to optimize fuel efficiency and exhaust gas emissions for different engine loads and speeds – if the exhaust gas composition is not prescribed by the exhaust gas aftertreatment system as for three-way catalysts used in today's gasoline engines. A lean premixed combustion process with λ>1, for example, would be interesting to increase fuel-efficiency in part load operation. However, exhaust gas pollutants, ammonia slip, and GHG emissions (nitrous oxide) cannot yet be investigated at the current test facility due to its special design and cyclic measurement operating procedure. Nonetheless, fundamental insight into the ignition process, the onset of combustion and burning characteristics including heat release can be gained from pressure and optical data.

For the variation of the premixed ammonia-air charge air-fuel equivalence ratio between λ = 1 and 2 both pilot injection time and duration were kept constant (see parameters in Table 4). This results in a pilot energy content between 0.9% for λ = 1 and 1.7% for λ = 2 in respect of the total energy available for combustion. Of course, those values are not necessarily transferable to genuine engines.

In Fig. 10 cylinder compression pressures and the corresponding (estimated) ammonia mixture charge temperatures are shown for the variation of the air-fuel equivalence ratio λ, investigated at operation

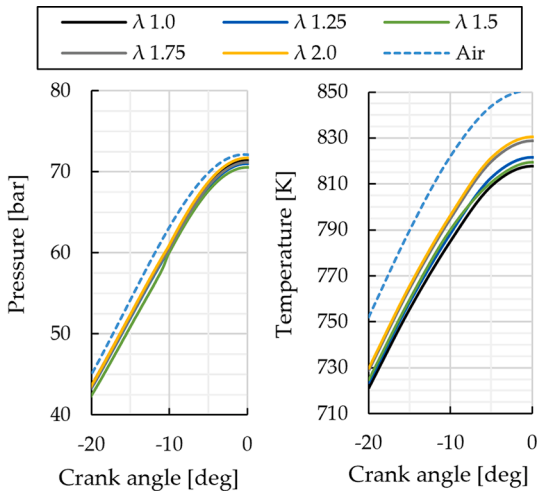

Fig. 10. Compression pressures p_{c_NH3} (measured, left) and temperatures T_{c_NH3} (calculated, right) of air vs. ammonia mixture for different air-fuel equivalence ratios λ at operation parameters p_c = 70 bar, T_{in} = 50 °C.

parameters p_c = 70 bar, and T_{in} = 50 °C. Adding more fuel in the premixed charge (lower λ) reduces both, compression pressure and tempe as expected. The reduction of compression pressure p_{c_NH3} and temperature T_{c_NH3} for varied air-fuel equivalence ratios λ was not compensated by adjusting intake boost pressure p_b and/or temperature T_{in}. The test rig was always operated with the defined reference values as described in section 2.3 (Table 3). Lower amounts of fuel result in lower cylinder peak pressures due to the reduced amount of energy available for combustion. Further, changes in the air-fuel equivalence ratio λ also influences the ignitability and the flame speed respectively combustion duration, so the peak pressure does not scale linearly with energy content.

Fig. 11 illustrates the combustion pressure traces over crank angle for different air-fuel equivalence ratios λ for a constant intake temperature of T_{in} = 50 °C, compression pressure of p_c = 70 bar, and pilot fuel injector energizing time of *ET* = 500 µs (*DOI* = 532 µs). In the leanest case (λ = 2), almost no pressure rise can be observed - it is difficult to see if any combustion takes place at all. The difference between the cases with λ = 1.25 and 1.5 appears to be rather large – originating from the specific test facility design, as discussed before (see Fig. 7) in section 3.1.

Fig. 12 shows the corresponding apparent heat release rates. As expected, at stoichiometric conditions (λ = 1.0) the *aHRR* reaches a maximum. For an air-fuel equivalence ratio of λ = 2, the *aHRR* indicates still a marginal combustion process taking place even though the pressure increase (see Fig. 11) is almost indiscernible. Another effect of the air-fuel equivalence ratio variation is the shorter ignition delay and faster rise of the *aHRR* in the very early combustion phase for leaner

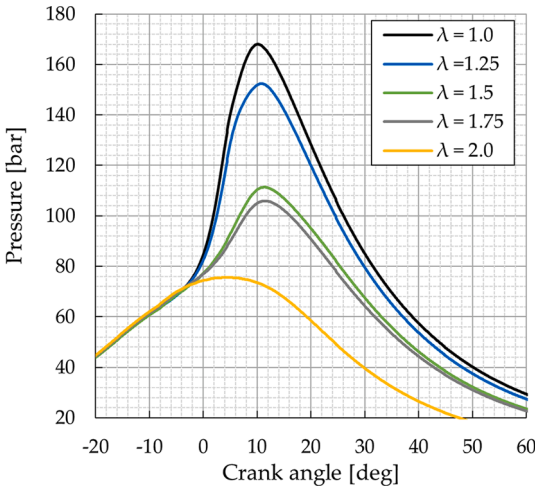

Fig. 11. NH_3 combustion pressure traces for different air-fuel equivalence ratios λ at operation parameters $p_c = 70$ bar, $T_{in} = 50$ °C, $SOI = -10$ °CA, and $ET = 500$ µs.

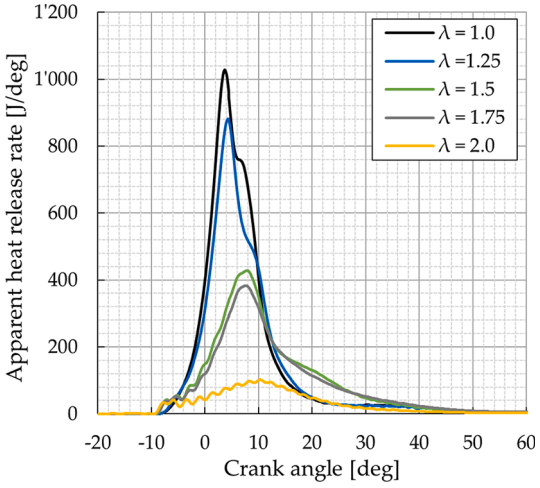

Fig. 12. Apparent heat release rate (aHRR) for different air-fuel equivalence ratios λ at operation parameters $p_c = 70$ bar, $T_{in} = 50$ °C, $SOI = -10$, and $ET = 500$ µs.

conditions. This can be attributed to the pilot spray ignition respectively combustion phase which is retarded by higher ammonia contents. For the two fuel richer cases ($\lambda = 1$ and $\lambda = 1.25$) the "staged" combustion as described in the comparison between methane and ammonia combustion in section 3.1 can be observed as well. For leaner conditions, the combustion is much slower, which results in a lower maximum *aHRR* that is reached at a later crank angle position. The combustion process is drawn out and extends far into the expansion stroke. The combined effect of the late maximum *aHRR*, the prolonged combustion, and the specific design of the test facility results in the large difference of the pressure traces for $\lambda = 1.25$ and 1.5 recognizable in Fig. 11.

As described in section 2.3, an apparent flame propagation speed s_{aFP} can be evaluated from the high-speed Schlieren measurements. The results in terms of air-fuel equivalence ratio λ variation are shown in Fig. 13. For short ignition delays it is difficult to differentiate the early flame from the evaporating pilot spray. However, after the combustion propagates into the premixed charge, the calculated values are quite stable. Whereas the apparent flame propagation speed s_{aFP} differs not much for the two fuel richer ammonia/air charges ($\lambda = 1$ and 1.25), the reduction for leaner mixtures ($\lambda \geq 1.5$) is clearly visible. The slow combustion of lean mixtures is not only reflected in the low apparent flame

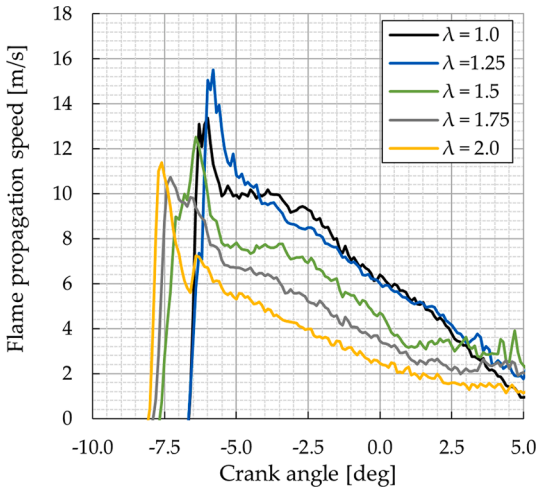

Fig. 13. Apparent flame propagation speed s_{aFP} of premixed ammonia dual-fuel combustion for different air-fuel equivalence ratios λ at operation parameters $p_c = 70$ bar, $T_{in} = 50$ °C, $SOI = -10$ °CA, and $ET = 500$ µs.

propagation speed s_{aFP} but also in its slow decline back to zero.

The ignition delay (*ID*) for different air-fuel equivalence ratios λ is difficult to discern exactly from the apparent heat release rate traces shown in Fig. 12. Thus, it is presented separately in Fig. 14 for both ID detection by way of the heat release rate calculation, and ID detection by analysis of the optical images (as described in section 2.2). Time is defined from the effective (hydraulic) start of the pilot fuel injection (*SOI*). The ignition delay values obtained from the *aHRR* calculation and from the image analysis are in good agreement. Clearly the ignition delay is longer for lower air-fuel equivalence ratios λ, longest at stoichiometric conditions. This can be attributed on one side to the retarding influence of ammonia on the ignition of the pilot fuel (as seen in methane dual-fuel combustion). On the other side, the high heat capacity of ammonia (which is almost three times higher than for air) will result in lower end of compression temperatures T_{c_NH3} for higher fuel contents (Fig. 10), which strongly influences the ignition delay. The transition time (defined in section 2.3) can be interpreted as the time required from ignition until the flame spreads out from the pilot fuel spray into the premixed charge. The retarding effect of ammonia content and temperature is less pronounced but nonetheless clearly observable with longer transition times for fuel richer mixtures.

Fig. 15 shows the superimposed Schlieren/OH* chemiluminescence

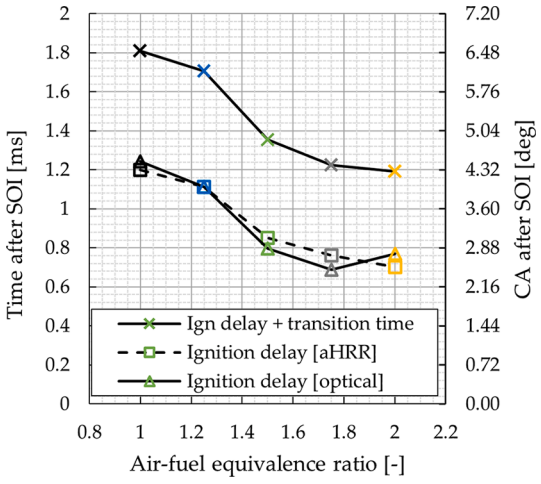

Fig. 14. Ignition delay and combustion transition time for different air-fuel equivalence ratios λ at operation parameters $p_c = 70$ bar, $T_{in} = 50$ °C, $SOI = -10$ °CA, and $ET = 500$ µs.

recordings for air-fuel equivalence ratio λ variation, images displayed in crank angle steps from −9 °CA to +2 °CA. The long ignition delay for fuel rich mixtures is clearly observable. In the stoichiometric case ($\lambda = 1$) the dodecane pilot spray is fully evaporated until −5 °CA, but a first flame kernel is only visible 1 °CA later. The observable characteristic disappearance of the Schlieren signal is attributed to the first stage ignition respectively heat release of the low-temperature combustion that compensates the refractive index change due to mixture cooling from fuel evaporation. Afterwards, the flame quickly propagates into the premixed charge surrounding the evaporated spray. Longer ignition delays also move the ignition location further away from the injector nozzle because the (evaporated) pilot fuel mixing with the premixed charge is still transported downwards due to the momentum from the injection. For fuel richer mixtures ($\lambda \leq 1.5$) at crank angle positions from 0 °CA onwards, transparent areas inside the reactive zones can be observed. These areas with very low variations of the refractive index (which causes Schlieren signal) are an indication of fairly homogeneous hot zones spanning the whole width between the windows of the optical combustion chamber. The images also indicate that there is a marginal combustion process taking place in the ammonia/air mixture surrounding the pilot spray for the leanest case with an air-fuel equivalence ratio of $\lambda = 2$ – in accordance with the heat release analysis results shown in Fig. 12.

Variation of start of pilot fuel injection

The start of pilot fuel injection was varied between $SOI = -20$ °CA and TDC at elsewise reference operation parameters, such as compression pressure $p_c = 70$ bar, intake temperature $T_{in} = 50$ °C, air-fuel equivalence ratio $\lambda = 1.5$, and injector energizing time $ET = 500$ µs. Depending on the time of injection, the pilot fuel is supplied into the premixed ammonia/air charge at different pressure and temperature levels. As recognizable by the pressure respectively temperature traces for $\lambda = 1.5$ in Fig. 10, this means that for an *SOI* of −20 °CA the pilot fuel is injected into the mixture under pressure respectively temperature states of about $p \approx 42$ bar and $T \approx 725$ K. At *TDC* the conditions for the mixture reveal approximately of $p \approx 70$ bar and $T \approx 810$ K. However, especially for very early injections, the ongoing compression stroke will increase pressure as well as temperature levels considerably during the fuel mixing process respectively between *SOI* and ignition.

The images in Fig. 16 show ignition and the early combustion process in steps of 0.8 °CA relative to the individual start of the pilot fuel injection. Clearly observable are the longer ignition delays for earlier pilot injections due to the lower pressure and temperature levels (see also ignition delays in Fig. 19). Longer delays also shift the position of ignition and the early combustion away from the pilot injector nozzle as seen before in the variation of the air-fuel equivalence ratio λ. The effect is also influenced by the charge density at the time of the pilot injection: Early fuel sprays can penetrate farther into the mixture due to the lower gas density.

Comparing images of the earliest injection time ($SOI = -20$ °CA) with the second earliest injection ($SOI = -15$ °CA) it is recognizable that the "combusted area" for the first case 7.4 °CA after *SOI* (i.e. at −12.6 °CA absolute) is about the same as the area of the second case 4.2 °CA after *SOI* (i.e. at −10.8 °CA absolute). Thus, pressure levels for the two cases should be about equal around crank angle of −11.5 °CA, as illustrated in Fig. 17. However, from then onwards the pressure traces deviate strongly – the pressure rises much faster for the earlier pilot injection at $SOI = -20$ °CA.

As illustrated in the corresponding apparent heat release rates shown in Fig. 18, the earliest pilot injection is indeed different from the other cases: It exhibits a slowly start, but then continuously accelerating *aHRR*. The other cases reveal an initially fast rising heat release rate followed by a short "plateau" before rising again, but less steeply. The behavior of the earliest *SOI* can be explained on one side by the temperature, which is not yet high enough for rapid combustion, and on the other side by the relatively lean dodecane/ammonia/air mixture at time of ignition due to the long ignition delay. For later *SOI*s however, temperature levels are higher, and dodecane/ammonia/air mixtures are richer at the time of ignition due to the shorter ignition delays. This results in a fast-rising *aHRR* that is, however, followed by a certain overswinging on the mentioned "plateau" before the heat releases rises again. This can be interpreted as a changeover delay to the purely premixed charge combustion.

Fig. 19 shows the analyzed ignition delays (optically and based on *aHRR*) for the *SOI* variation. As expected, for earlier *SOI*s the *ID* increases due to lower temperature operation conditions. The three later *SOI*s = −10/−5/0 °CA reveal ignition delays of about the same order of magnitude with *ID*≈0.65 – 0.75 ms. Thus, due to almost equal timing in terms of pilot fuel ignition respectively similar mixture conditions for

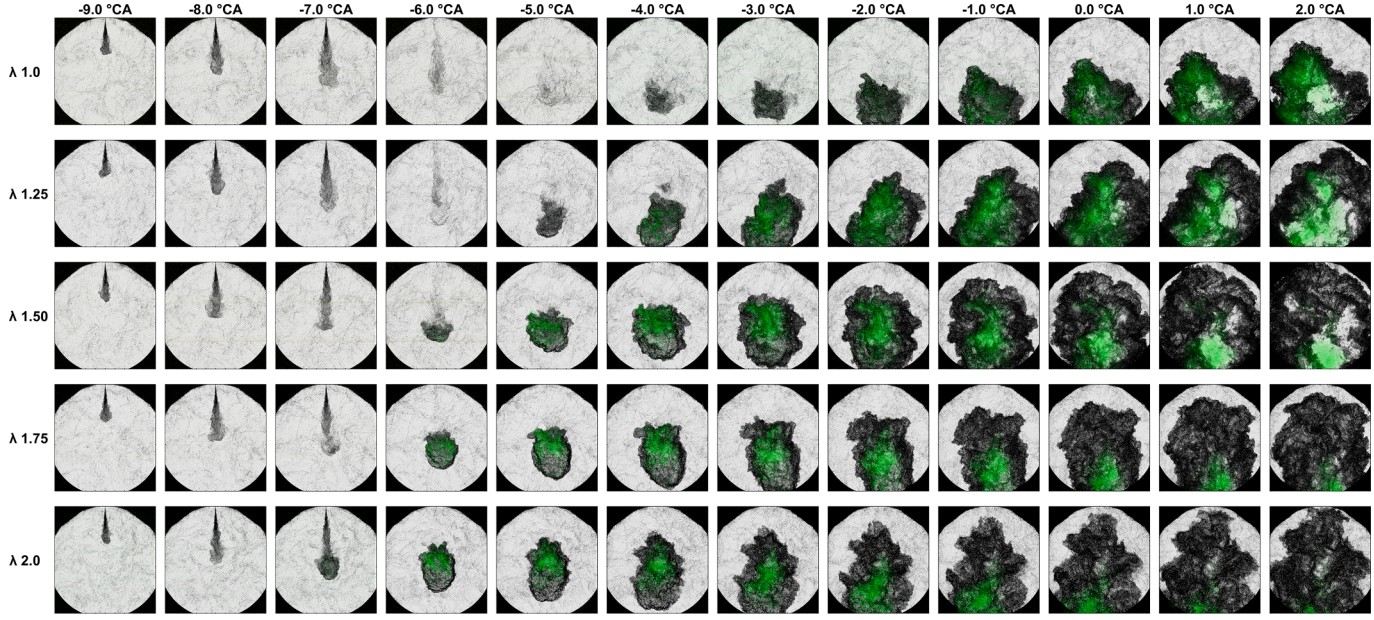

Fig. 15. Overlayed image sequences of simultaneously acquired high-speed Schlieren/OH*chemiluminscence recordings of pilot fuel ignited ammonia DF combustion for different air-fuel equivalence ratios λ at operation parameters $p_c = 70$ bar, $T_{in} = 50$ °C, $SOI = -10$ °CA, and $ET = 500$ µs.

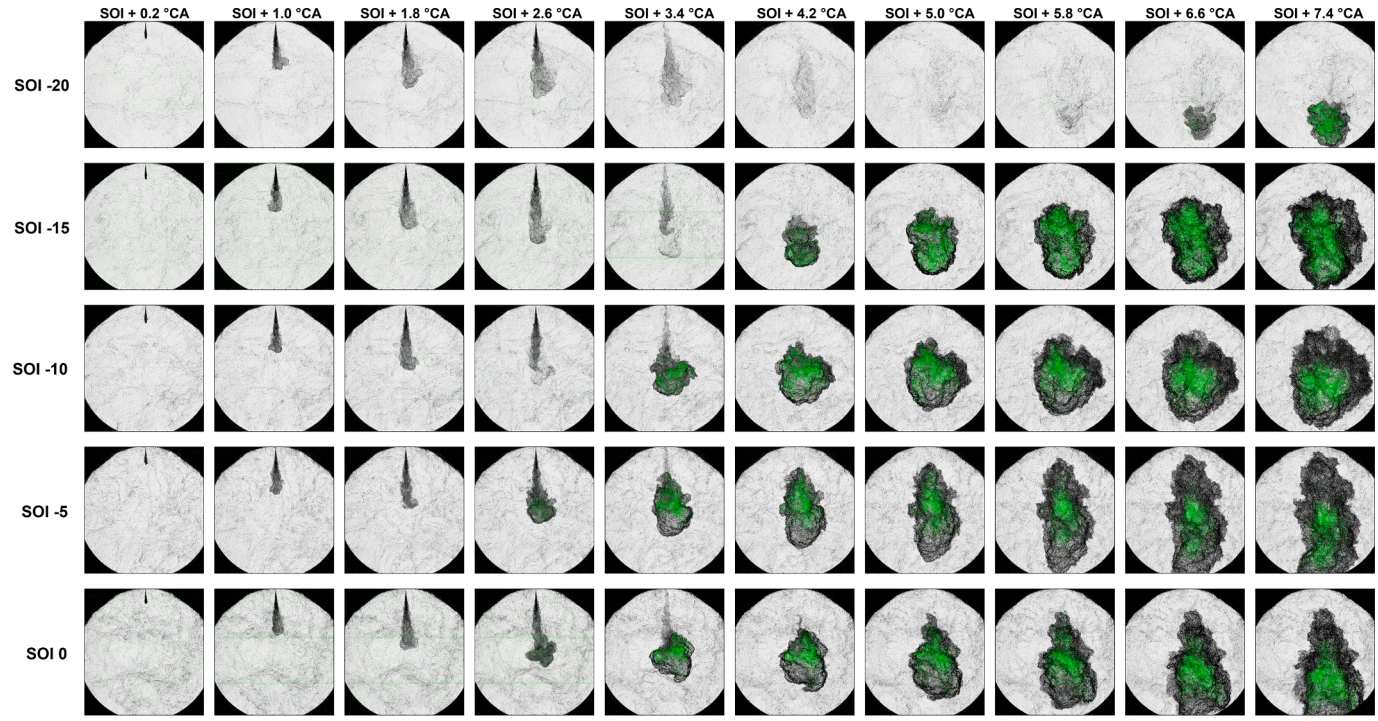

Fig. 16. Overlayed image sequences of simultaneously acquired high-speed Schlieren/OH*chemiluminscence recordings of pilot fuel ignited ammonia DF combustion for different start of pilot fuel injection *SOI* at operation parameters $p_c = 70$ bar, $T_{in} = 50$ °C, $\lambda = 1.5$, and $ET = 500$ µs.

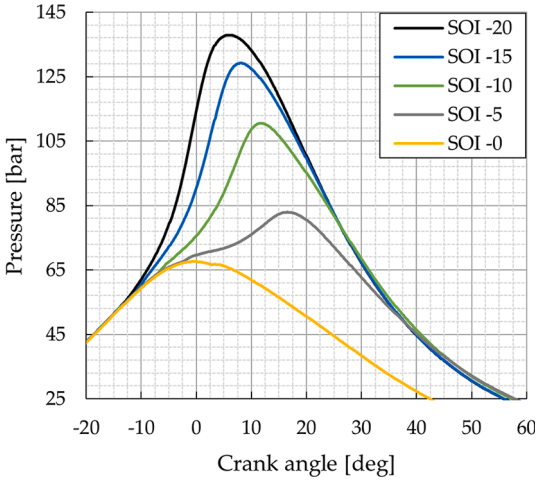

Fig. 17. Combustion pressure for the given *SOI-variation* at operation parameters $p_c = 70$ bar, $T_{in} = 50$ °C, $\lambda = 1.5$, $SOI = -10$ °CA, and $ET = 500$ µs.

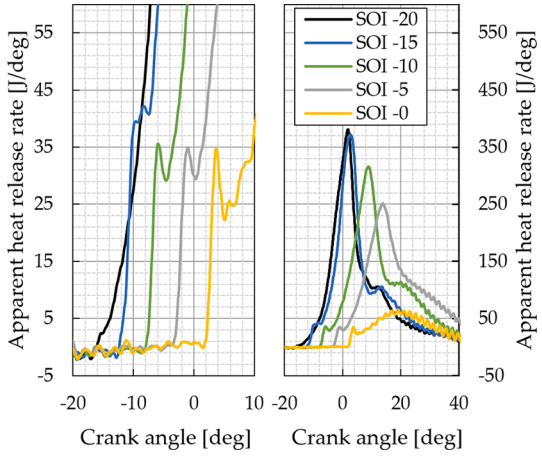

Fig. 18. Apparent heat release rate *aHRR* as close-up (left) and full-view (right) for the given *SOI*-variation at operation parameters $p_c = 70$ bar, $T_{in} = 50$ °C, $\lambda = 1.5$, and $ET = 500$ µs.

the spray, the *aHRR* (see Fig. 18) exhibits a comparable behavior. The transition time (see section 2.3) for those three later *SOI*s of about 0.9 ms≈3.2 °CA (estimated from Fig. 19) could be interpreted as delay between pilot fuel ignition and the again rising heat release rate after the "plateau" (combustion transition). For the $SOI = -15$ °CA case, the ignition delay is markedly longer ($ID \geq 1$ ms) and thus affecting combustion transition respectively *aHRR* due to increased amount of ammonia entrained into the igniting spray. The earliest pilot injection ($SOI = -20$ °CA) that exhibits a long ignition delay and a slowly starting combustion has the effect that the burned volume at the time when the pilot fuel is fully consumed is considerably larger. This promotes faster combustion of the remaining pure premixed charge and results in a more rapid rise of the pressure.

The peak pressures shown in Fig. 17 are moved to later crank angles for later pilot injection times as expected, and for the latest pilot injection time (at *TDC*) there is hardly any pressure increase observable. However, the images in Fig. 16 and the corresponding apparent heat release rate in Fig. 18 prove that even in this case combustion is present. The prolonged "plateau" phase in the *aHRR* (in comparison to cases with earlier injection times), which is also reflected in the slightly longer transition time in Fig. 19, are an indication of the quickly worsening conditions for the combustion of the premixed charge due to the dropping temperature level in the expansion stroke.

As mentioned in section 3.1 the specific design of the test rig has a strong influence on the late combustion phase, therefore direct comparisons of heat release for different measurement conditions are difficult. However, since the total energy content has been kept constant for this comparison, the apparent heat releases are shown in Fig. 20. As seen in the pressure traces, earlier pilot injection times lead to an earlier release of the energy. Since the temperature of the unburned zones rises

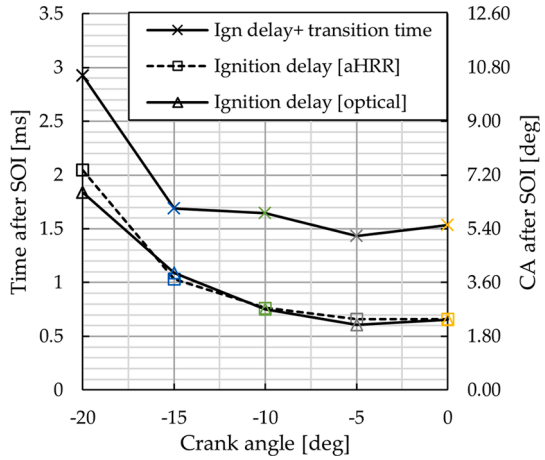

Fig. 19. Ignition delay for *SOI* variation in 5 °CA steps from −20 °CA to TDC at operation parameters $p_c = 70$ bar, $T_{in} = 50$ °C, $\lambda = 1.5$, and $ET = 500$ µs.

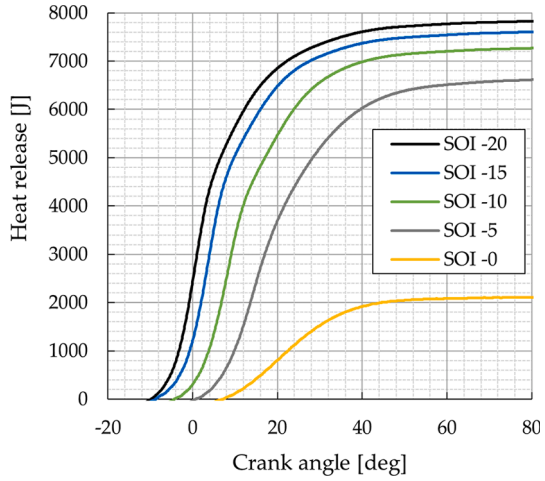

Fig. 20. Apparent heat release *aHR* over crank angle for different *SOI* at operation parameters $p_c = 70$ bar, $T_{in} = 50$ °C, $\lambda = 1.5$, and $ET = 500$ µs.

on one side with the pressure increase from combustion but decreases on the other side due to the starting expansion stroke, a late and/or slow combustion will be detrimental for a complete energy conversion. For the latest pilot fuel injection (at *TDC*), which exhibits the slowest combustion and almost no pressure increase, this results in an almost complete end of *aHR* after 40 °CA. For earlier pilot injection times this effect is less pronounced, but limits the totally converted energy, nonetheless.

The apparent flame propagation speed for the *SOI* variation is illustrated in Fig. 21. The earliest pilot injection (*SOI* = −20 °CA), featuring a slowly rising *aHRR* as seen in Fig. 18, needs a longer time to reach the maximum s_{aFP} here as well in comparison to the other *SOI* cases. Later pilot injection times show comparable characteristics, but with a trend towards slower propagation speeds for later *SOI*s. This corresponds to less steep rising of *aHR*s as shown in Fig. 20. The analysis of the apparent flame propagation speed ends when combustion covers most of the optically accessible combustion chamber. For the cases with pilot injection at *SOI*s of −5 °CA and *TDC* this does not happen until 20 °CA, but the flame propagation speed drops towards zero due to the dropping temperature levels in the expansion stroke. It must be noted that the changing volume due to the ongoing compression respectively expansion stroke has an influence on the apparent flame propagation speed. Due to the fast start of combustion with high initial s_{aFP} this effect is weak in the compression stroke, but it can lead to an overestimation of low apparent flame propagation speeds in the expansion stroke.

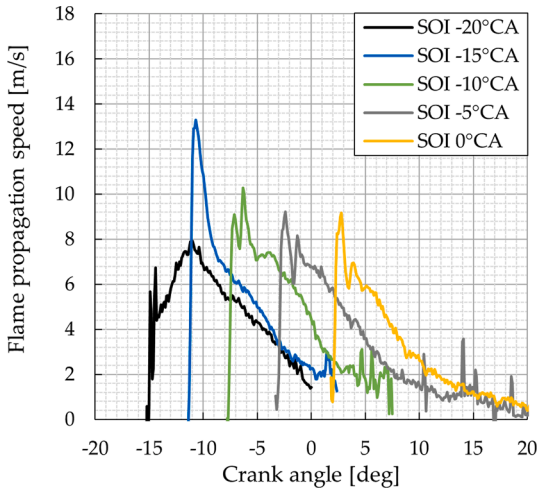

Fig. 21. Apparent flame propagation speed s_{aFP} over crank angle for different *SOI* at operation parameters $p_c = 70$ bar, $T_{in} = 50$ °C, $\lambda = 1.5$, and $ET = 500$ µs.

The variation of the pilot injection time shows that an early pilot injection time is necessary for an efficient ammonia combustion due to the inherently slow ignition and combustion process. In genuine engines, of course, the optimization of the pilot injection time is also influenced by other factors like ignitability, cyclic variability, maximum pressure rises rates, and emissions.

Variation of operation parameters

Conditions for mixing- and ignition processes of pilot fuel and premixed charge can also be influenced by varying intake pressure and/or temperature. For the first case, a *SOI* variation as shown in section 3.3 was investigated for a higher intake temperature of $T_{in} = 100$ °C with an unchanged compression pressure of $p_c = 70$ bar. For the second case, the intake temperature of $T_{in} = 50$ °C was kept unchanged, but the intake boost pressure p_b was adjusted accordingly (see Table 3) to reach compression pressures of $p_c = 100$ bar respectively $p_c = 130$ bar. All other operation parameters were kept constant with $\lambda = 1.5$, *SOI* = −10 °CA, and $ET = 500$ µs. The corresponding pressure and estimated temperature traces are shown in Fig. 22.

A higher intake temperature of $T_{in} = 100$ °C with the reference

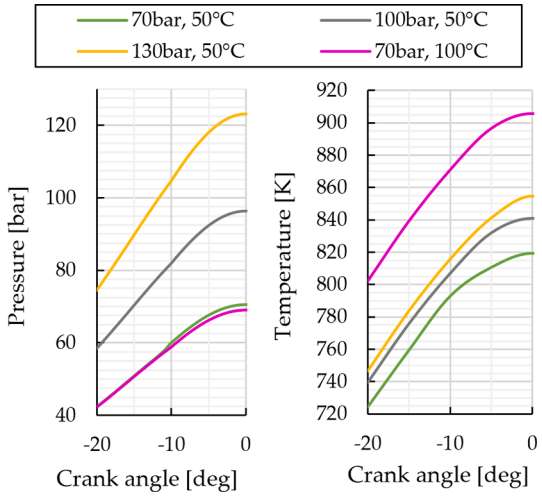

Fig. 22. Compression pressures (measured) and temperatures (calculated) of ammonia mixture charges for a variation of compression pressures p_c and intake temperatures T_{in} at operation parameters $\lambda = 1.5$, *SOI* = −10 °CA, and ET = 500 µs.

compression pressure $p_c = 70$ bar increases the peak compression temperature by 85 °C. The two higher compression pressures at the standard intake temperature of $T_{in} = 50$ °C results in slightly higher compression temperatures T_c.

The pressure traces for the first case with a variation of *SOI* are shown in Fig. 23. The drawn lines represent all measured cases for an intake temperature of $T_{in} = 100$ °C; the dashed lines for *SOI* = −20 /−10/0 °CA are the corresponding pressure traces of the intake temperature $T_{in} = 50$ °C cases presented in Fig. 17. Higher reactivity in the hotter environment is reflected in a shorter ignition delay (see also Fig. 25), a faster pressure rises rate and a higher peak combustion pressure. This effect is stronger for late pilot injections: whereas the pressure increases for a *SOI* = 0 °CA was almost indiscernible for an intake temperature of $T_{in} = 50$ °C – combustion in the hotter environment is late, but clearly recognizable. Even the two (very) late pilot injection at *SOI* = +2.5/+5 °CA show a pressure increase due to combustion, in the colder case with $T_{in} = 50$ °C however no ignition could be observed.

The corresponding apparent heat releases shown in Fig. 24 confirms the findings – the *aHR* starts earlier and rises faster in the hotter environment for equal pilot injection times. As expected, the total energy conversion is also improved by higher temperatures, even late *SOI*s of *SOI* = 0/5 °CA can convert most of the energy contained in the fuel.

The "kink" in the *aHR* trace around TDC for *SOI* = −20 °CA (and to less extent around 8 °CA for *SOI* = −10 °CA) is again the effect of the special test facility design with its split combustion volumes as described in section 3.1. Late pilot injection times, or a colder environment, results in lower combustion speeds, hence the effect is smaller and not observable in the apparent heat release traces.

Ignition delays for the second case featuring different inlet conditions (pressures and temperatures), but with constant start of injection of *SOI* = −10 °CA are shown in Fig. 25. As expected, both higher intake temperatures and boost pressures (leading to increased compression pressures) reduce the *ID*. For the colder case with $T_{in} = 50$ °C, a pressure variation (at *SOI*) between $p = 60$ bar and $p = 105$ bar (for the corresponding compression pressures of $p_c = 70$ bar and $p_c = 130$ bar) has about the same effect as an increase of temperature *T* (at *SOI*) by about 85 °C (for intake temperatures $T_{in} = 50$ °C respectively $T_{in} = 100$ °C).

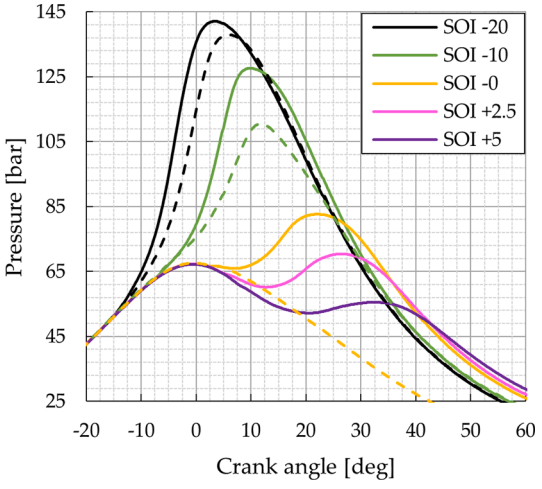

Fig. 23. Combustion pressure for different *SOI* at compression pressure $p_c = 70$ bar for intake temperatures $T_{in} = 100$ °C (drawn lines) vs. $T_{in} = 50$ °C (dashed line) at operation parameters $\lambda = 1.5$, *SOI* = −10 °CA, and *ET* = 500 µs.

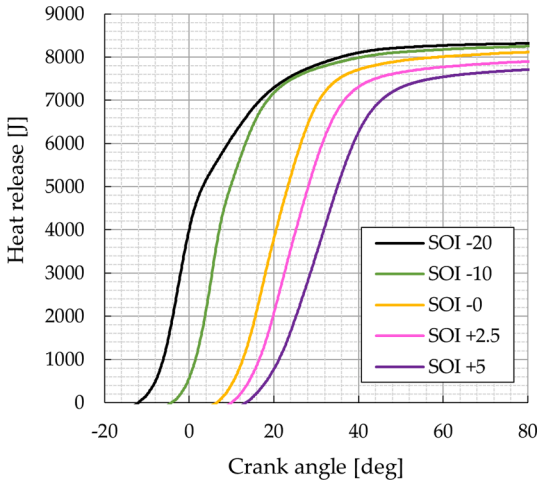

Fig. 24. Apparent heat release *aHR* for different *SOI* at intake operation conditions of $p_c = 70$ bar, and $T_{in} = 100$ °C (instead of $T_{in} = 50$ °C) at operation parameters $\lambda = 1.5$, *SOI* = −10 °CA, and *ET* = 500 µs.

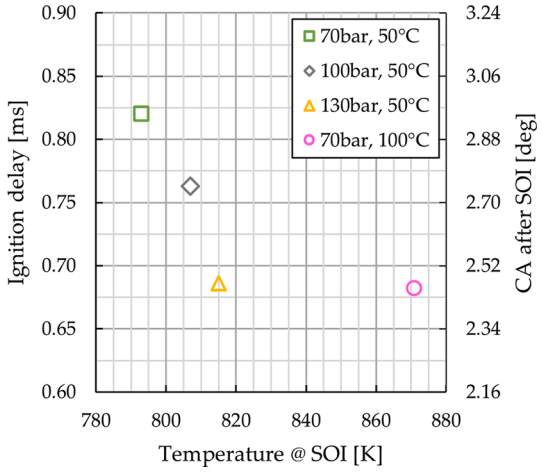

Fig. 25. Ignition delay dependence of temperature *T* at *SOI* = −10 °CA by variation of compression pressure p_c and intake temperature T_{in} at operation parameters $\lambda = 1.5$, and *ET* = 500 µs.

Conclusions

The novel optically accessible test facility "Flex-OeCoS" has been successfully adapted enabling pilot fuel ignited ammonia/air-premixed dual-fuel combustion process investigations in terms of ignition and combustion characteristics. It features IC engine relevant operation conditions such as pressures, temperatures, and flow (turbulence) conditions as well as adjustable mixture charge composition and pilot fuel injection settings. Acquisition of boundary conditions and operating parameters by comprehensive instrumentation allows a thermodynamic analysis of the combustion. Simultaneously applied high-speed Schlieren/OH* chemiluminescence measurements complete the examination of processes inside the combustion chamber. Within a parameter variation of air-fuel equivalence ratio, start of pilot fuel injection, and pressure/temperature operation conditions ignition delay, dual-fuel combustion transition behavior, and turbulent flame propagation as well as corresponding heat release have been investigated.

Initially a representative dodecane pilot fuel ignition ammonia dual-fuel process has been compared to methane DF combustion at equivalent operation conditions such as air-fuel ratio, compression pressure and temperature and pilot fuel supply. In terms of heat release based on different fuel properties, such as lower heating value and air-fuel ratio

partly compensating each other, the resulting energy content of the ammonia/air mixture was 4.6% lower than the one for the me-thane case. Accordingly, corresponding peak pressures and heat release were established. The ignition delay of the dodecane pilot fuel seems to be quite similar for both cases. However, due to the higher reactivity of the methane/air mixture the heat release rate rises faster in the initial combustion phase. The combustion transition respectively inflammation of the premixed charge is deferred in the ammonia case, reflecting the lower reactivity.

Variation of air-fuel equivalence ratio, start of pilot fuel injection, and compression pressure respectively temperature was investigated for premixed ammonia dual-fuel combustion initiated by dodecane pilot fuel. Adding more fuel in the premixed charge reduces both compression pressure and particularly temperature, thus increasing ignition delay and deferring heat release in the very early combustion phase. On the other hand, larger energy content leads to correspondingly higher heat release rate respectively pressure rise with higher peak levels, and faster flame propagation. Variation of start of pilot fuel injection from earlier crank angle towards TDC establishes shorter ignition delay (due to higher compression temperatures), but retards center of combustion position, affecting pressure rise respectively heat release in the expansion phase. Process boundary operation conditions in terms of higher compression pressures and intake temperature were varied to complete the investigation. As expected, ignition delay decreases, and higher chemical reactivity is established. Varying the start of injection with corresponding compression pressure and temperature further illustrated the strong temperature dependence in terms of ignition delay, heat release (peak pressure), and center of combustion position. The investigations performed under engine relevant operation conditions demonstrate combustion control possibilities and limits of applicability. These findings corroborate the applicability of premixed ammonia dual-fuel combustion process in view of genuine engines.

The findings of the optical investigations carried out in parallel confirm the thermodynamic analysis and promote an assessment of the processes taking place. In particular, pilot fuel evaporation and auto-ignition, combustion transition into premixed ammonia charge, and flame propagation are visualized. Moreover, an apparent flame propagation speed could be evaluated, enabling a comparison within operation parameter variation.

Based on first promising results further investigations are planned. A major necessity relates to a test facility extension in view of emission measurements. In the context of combustion characteristics, a critical point (besides ammonia slip itself) is the expected nitrous oxide emission, which as an extremely harmful climate gas. Moreover, pilot fuel injection mass variation with respect to ignition delay (DOI>ID) is of interest. Additional fuel added into the combustion zone would increase mixing, thereby stabilizing early combustion phase, and thus, affecting heat release and cycle-to-cycle stability.

Declaration of Competing Interest

We have no conflicts of interest to disclose.

Acknowledgements

Financial support from the Swiss Federal Office of Energy(SFOE contract SI/502152–01) as well as co-funding by WinGD is gratefully acknowledged.

Supplementary materials

Supplementary material associated with this article can be found, in the online version, at doi:10.1016/j.jfueco.2022.100074.

References

[1] United Nations, "*Paris Agreement*", 2015, http://unfccc.int/files/essential_background/convention/application/pdf/english_paris_agreement.pdf.
[2] "*Maritime Forecast to 2050*", Energy Transition Outlook 2020, DNV (Det Norske Veritas) 2022.
[3] Statista, "*Ammonia production worldwide from 2010 to 2020*", 2022. https://www.statista.com/statistics/1266378/global-ammonia-production/.
[4] Dimitriou P, Javaid R. A review of ammonia as a compression ignition engine fuel. Int J Hydrogen Energy Feb. 2020;45(11):7098–118. https://doi.org/10.1016/j.ijhydene.2019.12.209.
[5] Valera-Medina A, et al. Review on ammonia as a potential fuel: from synthesis to economics. Energy Fuels May 2021;35(9):6964–7029. https://doi.org/10.1021/acs.energyfuels.0c03685.
[6] E. Kroch, "Journal of the institute of petroleum", pp. 213–23, 1945.
[7] Rosenthal AB. Energy depot – a concept for reducing the military supply burden. SAE Technical Papers; 1965. https://doi.org/10.4271/650050.
[8] Cornelius W, Huellmantel LW, Mitchell HR. Ammonia as an engine fuel. SAE Technical Papers; 1965. https://doi.org/10.4271/650052.
[9] Gray JT, Dimitroff E, Meckel NT, Quillian RD. Ammonia Fuel - Engine Compatibility and Combustion. SAE Technical Papers 660156; 1966. https://doi.org/10.4271/660156.
[10] Pearsall TJ, Garabedian CG. Combustion of Anhydrous Ammonia in Diesel Engines. SAE Technical Paper 670974; 1967. https://doi.org/10.4271/670947.
[11] Cheddie D. Ammonia as a Hydrogen Source for Fuel Cells: a Review. Hydrogen energy – challenges and perspectives. InTech; 2012. p. 75–100.
[12] Lucentini I, Garcia X, Vendrell X, Llorca J. Review of the Decomposition of Ammonia to Generate Hydrogen. Ind Eng Chem Res Dec. 2021;60(51):18560–611. https://doi.org/10.1021/acs.iecr.1c00843.
[13] J. Schramm, J.N. Klüssmann, L.R. Ekknud, and A. Ivarsson, "*Ammonia Application in IC Engines*", 2020.
[14] Mounaïm-Rousselle C, Bréquigny P, Dumand C, Houillé S. Operating limits for ammonia fuel spark-ignition engine. Energies Jul. 2021;14(14):4141. https://doi.org/10.3390/en14144141.
[15] Lhuillier C, Brequigny P, Contino F, Mounaïm-Rousselle C. Experimental study on ammonia/hydrogen/air combustion in spark ignition engine conditions. Fuel Jun. 2020;269:117448. https://doi.org/10.1016/j.fuel.2020.117448. February.
[16] McAllister S, Chen J-Y, Fernandez-Pello AC. Fundamentals of combustion processes: appendix. New York, NY: Springer New York; 2011.
[17] Frankl S, Gleis S, Karmann S, Prager M, Wachtmeister G. Investigation of ammonia and hydrogen as CO2-free fuels for heavy duty engines using a high-pressure dual-fuel combustion process. Int J Engine Res Oct. 2021;22(10):3196–208. https://doi.org/10.1177/1468087420967873.
[18] Han D, Liu Y, Huang Z. The Use of Ammonia as a Fuel for Combustion Engines. Engines and fuels for future transport. Singapore: Springer Singapore; 2022. p. 233–56. G. Kalghatgi, A. K. Agarwal, F. Leach, and K. Senecal, editors.
[19] Mounaïm-Rousselle C, Brequigny P. Ammonia as fuel for low-carbon spark-ignition engines of tomorrow's passenger cars. Front Mech Eng Sep. 2020;6:1–5. https://doi.org/10.3389/fmech.2020.00070. September.
[20] Chiong M-C, et al. Advancements of combustion technologies in the ammonia-fueled engines. Energy Convers Manag Sep. 2021;244:114460. https://doi.org/10.1016/j.enconman.2021.114460. April.
[21] Boretti A. Novel dual-fuel diesel-ammonia combustion system in advanced TDI engines. Int J Hydrogen Energy Mar. 2017;42(10):7071–6. https://doi.org/10.1016/j.ijhydene.2016.11.208.
[22] Reiter AJ, Kong S-C. Demonstration of compression-ignition engine combustion using ammonia in reducing greenhouse gas emissions. Energy Fuels Sep. 2008;22(5):2963–71. https://doi.org/10.1021/ef800140f.
[23] Reiter AJ, Kong S-C. Combustion and emissions characteristics of compression-ignition engine using dual ammonia-diesel fuel. Fuel Jan. 2011;90(1):87–97. https://doi.org/10.1016/j.fuel.2010.07.055.
[24] Niki Y, Yoo D-H, Hirata K, Sekiguchi H. Effects of ammonia gas mixed into intake air on combustion and emissions characteristics in diesel engine. In: ASME 2016 Internal Combustion Engine Division Fall Technical Conference; 2016. p. 1–6. https://doi.org/10.1115/ICEF2016-9364.
[25] Niki Y, Nitta Y, Sekiguchi H, Hirata K. Diesel fuel multiple injection effects on emission characteristics of diesel engine mixed ammonia gas into intake air. J Eng Gas Turbines Power Jun. 2019;141(6):1–7. https://doi.org/10.1115/1.4042507.
[26] Yousefi A, Guo H, Dev S, Liko B, Lafrance S. Effects of ammonia energy fraction and diesel injection timing on combustion and emissions of an ammonia/diesel dual-fuel engine. Fuel Apr. 2022;314:122723. https://doi.org/10.1016/j.fuel.2021.122723. December 2021.
[27] Yousefi A, Guo H, Dev S, Lafrance S, Liko B. A study on split diesel injection on thermal efficiency and emissions of an ammonia/diesel dual-fuel engine. Fuel May 2022;316:123412. https://doi.org/10.1016/j.fuel.2022.123412. January.
[28] Pochet M, Jeanmart H, Contino F. A 22:1 compression ratio ammonia-hydrogen HCCI Engine: combustion, load, and emission performances. Front Mech Eng Jun. 2020;6:1–16. https://doi.org/10.3389/fmech.2020.00043. X.
[29] Schneider B, Schürch C, Boulouchos K, Herzig S, Hangartner M, Humair D, Wüthrich S, Gossweiler C, Herrmann K. The Flex-OeCoS – a novel optically accessible test rig for the investigation of advanced combustion processes under engine-like conditions. Energies 2020;13(7):1794. https://doi.org/10.3390/en13071794.
[30] Wüthrich S, Humair D, Herrmann K, Bertola A. Enhanced instrumentation of an optical research engine with unique combustion chamber. In: 14th Int. AVL Symposium on Propulsion Diagnostics; 2020. June 23-24ISBN 978-3-9816971-6-2.

[31] Humair D, Cartier P, Süess P, Wüthrich S, Herrmann K, Barro C, Schneider B, Schürch C, Boulouchos K. Characterization of dual-fuel combustion processes. In: Rostock 6th Large Engine Symposium; 2020. September 3-4ISBN 978-3-941554-22-1.
[32] Vera-Tudela W, Schneider B, Wüthrich S, Herrmann K. Study on the ignitability of a high-pressure direct-injected methane jet using a diesel pilot, a glow-plug and a prechamber. Int J Engine Res 2021. https://doi.org/10.1177/14680874211048144. IJER-21-0139.
[33] Desantes JM, García-Oliver JM, Vera-Tudela W, López-Pintor D, Schneider B, Boulouchos K. Study of the auto-ignition phenomenon of PRFs under HCCI conditions in a RCEM by means of spectroscopy. Appl Energy 2016;179:389–400. https://doi.org/10.1016/j.apenergy.2016.06.134.
[34] Najafabadi MI, Egelmeers L, Somers B, et al. The influence of charge stratification on the spectral signature of partially premixed combustion in a light-duty optical engine. Appl Phys B 2017;123:108. https://doi.org/10.1007/s00340-017-6688-9.
[35] Srna A, Bolla M, Wright YW, Herrmann K, Bombach R, Pandurangi SS, Boulouchos K, Bruneaux G. Ignition characteristics of n-dodecane pilot fuel spray in a premixed compressed methane/air charge. Proc Combust Inst 2019;37:4741–9. https://doi.org/10.1016/j.proci.2018.06.177.
[36] Desantes JM, Pastor JV, García-Oliver JM, Vera-Tudela W. An experimental study of the effects of fuel properties on reactive spray evolution using Primary Reference Fuels. Fuel 2016;163:260–70. https://doi.org/10.1016/j.fuel.2015.09.064.
[37] Srna A, Bombach R, Herrmann K, Bruneaux G. Characterization of the spectral signature of dual-fuel combustion luminosity: implications for evaluation of natural luminosity imaging. Appl Phys B 2019;125:120. https://doi.org/10.1007/s00340-019-7222-z.
[38] Desantes JM, García-Oliver JM, Vera-Tudela W, López-Pintor D, Schneider B, Boulouchos K. Study of ignition delay time and generalization of auto-ignition for PRFs in a RCEM by means of natural chemiluminescence. Energy Convers Manage 2016;111:217–28. https://doi.org/10.1016/j.enconman.2015.12.052.
[39] Obrecht P. WEG: calculation of the heat development law based on measured combustion chamber pressure traces. In: in-house Thermodynamic Model, ETHZ-LAV & FHWN-ITFE; 2021.
[40] Seddik O. Development and Validation of a Micro-piloted Dual-fuel Combustion Model Based on Flamelet Generated Manifolds. ETH No. 28189. 2022.
[41] Schlatter S, Schneider B, Wright YM, Boulouchos K. N-heptane micro pilot assisted methane combustion in a Rapid Compression Expansion Machine. Fuel 2016;179:339–52. https://doi.org/10.1016/j.fuel.2016.03.006. Volume.
[42] Humair D. Characterization of dual-fuel combustion processes. University of Applied Sciences and Arts Northwestern Switzerland; 2022. FHNW–ITFE MSE Master Thesis.